RSC Advances

PAPER

View Article Online
View Journal | View Issue

Cite this: *RSC Adv.*, 2023, **13**, 15926

Insight into the direct conversion of methane to methanol on modified ZIF-204 from the perspective of DFT-based calculations†

Thong Nguyen-Minh Le, *[ab] Thu Bao Nguyen Le, [bc] Phat Tan Nguyen, [bd] Trang Thuy Nguyen, [e] Quang Ngoc Tran, [ab] Toan The Nguyen, [e] Yoshiyuki Kawazoe, [fgh] Thang Bach Phan [ab] and Duc Manh Nguyen [i]

Direct oxidation of methane over oxo-doped ZIF-204, a bio-mimetic metal–organic framework, is investigated under first-principles calculations based on density functional theory. In the pristine ZIF-204, the tetrahedral methane molecule anchors to an open monocopper site *via* the so-called η^2 configuration with a physisorption energy of 0.24 eV. This weak binding arises from an electrostatic interaction between the negative charge of carbon in the methane molecule and the positive Cu^{2+} cation in the framework. In the modified ZIF-204, the doped oxo species is stabilized at the axial position of a CuN_4-base square pyramid at a distance of 2.06 Å. The dative covalent bond between Cu and oxo is responsible for the formation energy of 1.06 eV. With the presence of the oxo group, the presenting of electrons in the O_p_z orbital accounts for the adsorption of methane *via* hydrogen bonding with an adsorption energy of 0.30 eV. The methane oxidation can occur *via* either a concerted direct oxo insertion mechanism or a hydrogen-atom abstraction radical rebound mechanism. Calculations on transition-state barriers show that reactions *via* the concerted direct oxo insertion mechanism can happen without energy barriers. Concerning the hydrogen-atom abstraction radical rebound mechanism, the C–H bond dissociation of the CH_4 molecule is barrierless, but the C–O bond recombination to form the CH_3OH molecule occurs through a low barrier of 0.16 eV. These predictions suggest the modified ZIF-204 is a promising catalyst for methane oxidization.

Received 21st April 2023
Accepted 15th May 2023

DOI: 10.1039/d3ra02650g

rsc.li/rsc-advances

1. Introduction

Conversion of methane to methanol remains an active research area for diversely beneficial purposes: (1) reducing the amount of greenhouse gas emission as methane, and (2) producing important chemical feedstock as methanol.[1–3] However, methane oxidation by chemical methods is challenging due to a prerequisite of high energy for a C–H bond dissociation (4.51 eV) and an overoxidation of the methanol product.[4] Traditional transition-metal and oxide-based catalysts have been extensively studied for methane conversion concerning their novel catalytic activities.[4–8] Methane molecules actively dissociate on transition metal surfaces. However, the combination of $-CH_3$ and –OH species to form methanol is a multiple-step process that is relatively ineffective and requires high temperatures.[4,5] All the above disadvantages also take place for the industrial-scale methanol synthesis through an indirect pathway by using a syngas, catalyzed by metal catalysts at temperatures of above 1000 °C.[3,5] Yet that synthesis is expensive and also produces abundant pollution by-products.

On the other hand, biological processes suggest a direct way to convert methane to methanol at low temperatures and high selectivity without releasing any byproducts.[2,3] It has been widely known that a class of bacteria so-called methanotrophs can directly oxidize methane to methanol in the presence of oxygen at ambient conditions relying on their soluble methane monooxygenase (sMMO) or particulate methane monooxygenase (pMMO) metalloenzymes.[3] Both enzymes are very reactive owing to the presence of containing metal active

[a]*Center for Innovative Materials and Architectures, Ho Chi Minh City 700000, Vietnam. E-mail: lnmthong@inomar.edu.vn*
[b]*Vietnam National University Ho Chi Minh City, Ho Chi Minh City 700000, Viet Nam*
[c]*Department of Mathematics and Physics, University of Information Technology, Ho Chi Minh City 700000, Viet Nam*
[d]*Department of Theoretical Physics, University of Science, Ho Chi Minh City 700000, Vietnam*
[e]*Key Laboratory for Multiscale Simulation of Complex Systems, University of Science, Vietnam National University – Hanoi, Hanoi 100000, Vietnam*
[f]*New Industry Creation Hatchery Center, Tohoku University, Sendai, 980-8579, Japan*
[g]*Department of Physics and Nanotechnology, SRM Institute of Science and Technology, Kattankulathur 603203, Tamil Nadu, India*
[h]*School of Physics, Institute of Science, Suranaree University of Technology, 111 University Avenue, Nakhon Ratchasima 30000, Thailand*
[i]*CCFE, United Kingdom Atomic Energy Authority, Abingdon, OX14 3DB, UK*

† Electronic supplementary information (ESI) available. See DOI: https://doi.org/10.1039/d3ra02650g

centers, *i.e.*, iron (Fe) for sMMO or copper (Cu) for pMMO. pMMO enzyme is found to be more popular in the methanotrophic bacteria family and more efficient for methane conversion than sMMO.[3,9] Therefore, pMMO attracts much interest in methane oxidation research. Theoretical modeling works on pMMO structures have demonstrated the significant reactivity of copper sites and clarified detailed mechanisms of methane conversion.[10,11] However, it is impossible to extract pMMO from bacteria for *in vitro* studies as well as for practical applications because it tends to lose its original catalytic activities. Therefore, various bioinspired catalytic materials have been proposed to enable direct methane–methanol conversion processes which are environment-friendly.

An attractive family of pMMO-mimetic materials is copper-exchanged zeolites. These materials are of high physical and chemical stability and exhibit significant activity for direct methane–methanol conversion at low temperatures.[12–17] Tricopper and dicopper sites in Cu–Na–ZSM-5 and Cu–H–ZSM-5 can activate methane at a high selectivity, low temperature (483–498 K), but low conversion rates.[12] Based on first-principles and microkinetic investigations, Engedahl *et al.* found that dicopper sites in Cu–SSZ-13 can dissociate C–H bonds at lower energy barriers under the influence of H_2O molecules.[16] Monocopper sites coordinated by four oxygen atoms in Cu_1/ZSM-5 exhibit high activity and selectivity for methane oxidation compared to most of the current noble metal catalysts.[17] However, monocopper sites in Cu–SSZ-13 are unfavorable for methane activation because of a high activation barrier of 1.14 eV.[13]

Metal–organic frameworks (MOFs), highly crystalline nanoporous structures, have been proposed as more efficient alternatives for mimicking biocatalysts of methane conversion.[1,18–22] MOFs have been utilized as catalysts or hosts for anchoring Cu-based complexes functionalizing as pMMO enzymes.[21] Mixed-valent Cu^+ and Cu^{2+} in tricopper[18] and dicopper[20] oxide clusters were embedded in NU-1000 MOFs. The combination of spectroscopic and activity experiments with DFT calculations demonstrated that such catalyst systems enable the direct methane–methanol conversion at mild conditions with a selectivity up to 70%.[18,20] A high selectivity of methanol was also reported for methane oxidation over active bis(μ-oxo) dicopper complexes ligated in MOF-808.[19] As opposed to monocopper centers in zeolites which do not activate methane efficiently, monocopper centers in MOFs are more promising. The combined theoretical and experimental study on the single-atom Cu-doped ZIF-7 evidenced a high-rate direct conversion through low activation energy barriers.[23] Recent experimental analyses and quantum calculations confirm the dominance of monocopper centers, coordinated by histidine-based imidazole ligands, for methane activation in the pMMO enzymes.[11] This finding drives research direction towards single-copper catalysts for direct methane–methanol conversions based on MOF structures.

ZIF-204 is a mixed-metal structure containing intrinsic monocopper active centers. It is stable in water solution and can separate CO_2 from CH_4 efficiently.[24] Additionally, their monocopper sites can coordinate dimethylformamide (DMF) molecules. In this work, ZIF-204 is chemically modified to mimic the pMMO environment by depositing oxo-oxidizing agents to monocopper sites. The oxidation of CH_4 by oxo center in ZIF-204 is investigated in terms of reaction paths, energy barriers of C–H bond dissociation and C–O bond recombination, and underlying electronic structure properties by theoretical calculations on the base of density functional theory (DFT). We aim to predict the potential energy surfaces and elucidate the catalytic activity for the methane oxidation over this bioinspired structure.

2. Computational methods

All the results are obtained from the spin-polarized density functional theory (DFT) calculations using the Vienna *Ab initio* Simulation Package (VASP 5.4.4).[25] The generalized gradient approximation functional of Perdew, Burke, and Ernzerhof's (PBE)[26,27] is employed with a D3 van der Waals correction.[28] The kinetic energy cutoff of 500 eV is used within the projected augmented wave (PAW)[29] pseudopotential. The criteria for electronic energy and force convergence are selected to be 10^{-6} eV and 0.01 eV $Å^{-1}$, respectively. The k-point mesh is sampled by Monkhorst–Pack grids at the Gamma point. The crystal structure of ZIF-204 is monoclinic with a unit cell containing 170 atoms. Its structural formula is $[C_{15}H_{15}N_{10}Cu_{1.5}Zn]_4$. The electron configurations of the metal ions have been assigned as Cu^{2+}: [Ar] $3d^9$ $4s^0$ and Zn^{2+}: [Ar] $3d^{10}$ $4s^0$. Taking into account strong correlations of electrons in d orbitals, Hubbard U correction of 5.5 eV is properly derived for Cu from the linear response method.[30] Detail of the method and *U* values is provided in Section S1 of the ESI.† For checking the performances of functionals, lattice parameters bench-marked with different functionals including LDA,[31] PBE,[26,27] revPBE,[32] RPBE,[33] PBE-D3,[26–28] and PBE-D3-U[26–28,30] are presented in Section S2 in the ESI.† Among tested functionals, PBE produces the most appropriate lattice constants and corresponding unit-cell volume in comparison to experimental values. Isolated molecules such as CH_4 are simulated inside a cubic box with a dimension of 20 Å. Functionalizing Cu center by an oxo group, the binding energy of this oxo ligand is defined

$$E_b = E_{host} + E_O - E_{host-O} \quad (1)$$

where E_{host}, E_O, and E_{host-O} are the total energies of the pristine host, the single O atom, and the host with a ligand O bound, respectively.

We formulate the adsorption energy ΔE_{ads} of a guest molecule X as following

$$E_{ads} = E_{host-X} - E_{host} - E_X \quad (2)$$

where E_{host-X}, E_{host}, and E_X are the total energies of the host structure with an adsorbed molecule X, the host structure without X, and the isolated X molecule, respectively.

The change of charge density due to the presence of a species X is determined as an electron density difference (EDD) $\Delta\rho$

$$\Delta\rho = \rho_{\text{host–X}} - \rho_{\text{host}} - \rho_{\text{X}} \quad (3)$$

where $\rho_{\text{host–X}}$, ρ_{host}, and ρ_{X} are the electron densities of the combined structure with the presence of both the host and X, of the host derived by the elimination of X, and of X derived by the elimination of the host, respectively. On creating individual components from the parent structure, the geometries of derived structures remain unchanged.

A computer program suite named LOBSTER (Local Orbital Basis Suite Towards Electronic-Structure Reconstruction) has been carried out to extract the electronic properties of the involved species.[34] Those calculations include the Mulliken charge and projected density of state (PDOS). The climbing image nudged elastic band (CI-NEB) method is also employed to evaluate energy barriers of the transition states along potential energy surfaces of conversion reactions.[35] For CI-NEB calculations, only atoms involved in considering reactions are relaxed, while the remaining atoms are frozen to reduce computational cost because they are almost unchanged during reactions. Derived transition states are confirmed by the fact that there has only one imaginary frequency for each transition state found. All atomic structures and EDD plots presented in this work are visualized by VESTA program, version 3.5.7.[36]

3. Result and discussion

3.1. Optimized structures

3.1.1. Pristine ZIF-204. The pristine ZIF-204, denoted as ZI hereafter, comprises single-atom transition metal nodes, *i.e.*, either Zn^{2+} or Cu^{2+}, coordinated by four imidazole linkers. The coordination symmetry at each node is tetrahedral for Zn and square planar for Cu, as shown in Fig. 1(a) The optimized structures show that the bond lengths of Zn and Cu with their imidazole linkers are almost the same, of about 2.00 Å and 1.98 Å, for Zn and Cu, respectively. Structural parameters at the Cu center are provided in Table 1. ZI is not a magnetic MOF, so its total spin is zero. While Zn^{2+} has a closed-shell configuration, Cu^{2+} remains to be spin-polarized cations due to their d electrons, as shown by PDOS in Fig. 4(b). Consequently, the antiferromagnetic configuration assigned to six Cu^{2+} cations in one unit cell is the most stable-optimized structure compared to ferromagnetic ones.

3.1.2. Modified ZIF-204. The oxo group is deposited onto the axial Cu site of the ZI, playing the role of an oxidant for the C–H σ-bond activation. The oxo-doped ZI structure is denoted as ZI_O hereafter which its oxo-containing fragment is shown in Fig. 1(b). Bond lengths and bond angles related to Cu center of the ZI_O are displayed in Table 1. There is a notable distortion of the geometry at the Cu site. Although bond lengths are not much different for ZI against ZI_O, bond angles become smaller in the ZI_O structure. The doped oxo ligand pulls the coordinated Cu atom out of its planar plane. It indicates that the original square planar symmetry turns into square-based pyramidal symmetry in the presence of the oxo group. We found that the doped oxo species locates above CuN4 surface and binds to Cu with a Cu–O bond length of 2.06 Å, and a binding energy of 1.06 eV. Mulliken charge distribution for both the ZI and ZI_O is shown in Table 2. All atoms in the ZI structure lose their negative charges upon the deposition of oxo onto Cu. Cu atom is most affected by losing about 0.17*e*, while it is only 0.04*e* lost on N atoms. The oxo has a negative charge of 0.50*e* induced by the coordination with Cu^{2+}. An EDD plot in Fig. 2 shows negative charge depletion and accommodation regions for Cu, N, and O, respectively. A high negative charge density between Cu and O indicates this is a type of dative covalent bond. PDOS in Fig. 4(c) shows this bond at around −4.0 eV represented by the overlapping of Cu_d and O_p orbitals. Additionally, there is also an extending of the negative charge region above the O atom, outside of the Cu–O bond, as shown in Fig. 2. This orbital corresponds to a crossing of a high density of state of O_p from −2.0 eV to 1.0 eV above the Fermi level, as plotted in Fig. 4(c). The abundance of negative charge in the oxo suggests that this is an active site for arriving adsorbates to adsorb and activate easily.

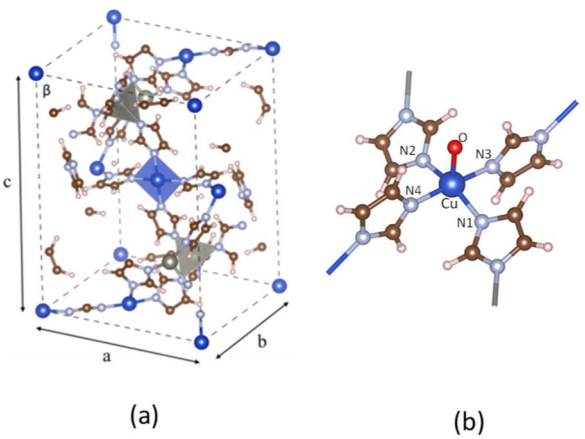

Fig. 1 The unit cell of the pristine ZI (a), the fragment of ZI_O (b). The spheres colored dark blue, gray, brown, light blue, red, and white represent Cu, Zn, C, N, O, and H atoms, respectively.

3.2. Adsorption of CH_4 over ZIF-204

3.2.1. CH_4 adsorption on ZI. Breakthrough experiments on methane uptake showed that ZIF-204 can capture methane with an uptake at about 13 $cm^3\ g^{-1}$, comparable to 22 $cm^3\ g^{-1}$ in BPL activated carbon.[24] This demonstrates the fact that ZIF-204 can adsorb methane at a considerable amount, *i.e.*, about half of the uptake of the industrial methane storage materials. The detail of methane adsorption on ZIF-204 has yet been addressed previously. Our calculated results show that methane stabilizes on the Cu site *via* the η^2 configuration, as shown in Fig. 3(a), with the adsorption energy of −0.24 eV, *cf.* Table 3, entry 1. At this configuration, the two hydrogen atoms are apart from the Cu with similar distances, *i.e.*, 3.02 and 3.35 Å, to minimize the repulsion between positive charges of Cu^{2+} site and the H atom. The electrostatic attraction mainly arises between the positive Cu^{2+} and the partial negative charge of the C atom (CH_4) indicated by an accommodation of negative charge between two atoms C and Cu^{2+} plotted in Fig. 3(b). The adsorption

Table 1 Bond lengths and bond angles related to the Cu center for both the ZI and ZI_O structures

	Bond length (Å)					Bond angle (°)	
Structure	Cu–O	Cu–N1	Cu–N2	Cu–N3	Cu–N4	N1–Cu–N2	N3–Cu–N4
ZI		1.98	1.98	1.97	1.97	180	180
ZI_O	2.06	2.01	1.99	1.90	1.90	157	174

Table 2 Mulliken charges of involved atoms around the Cu center. The sign (−) or (+) in front of bold numbers represent the loss or gain of negative charges (*e*) of that atom upon the functionalization with the oxo group, respectively

	Mulliken charge					
Structure	Cu	N1	N2	N3	N4	O
ZI	+1.28	−0.63	−0.63	−0.59	−0.59	
ZI_O	+1.45	−0.59	−0.59	−0.55	−0.53	−0.50
Lost(−)/gain(+) (*e*)	**−0.17**	**−0.04**	**−0.04**	**−0.04**	**−0.06**	**+0.50**

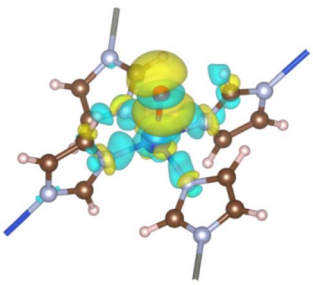

Fig. 2 EDD for the formation of the oxo ligand. The regions encoded by yellow and cyan stand for electron accumulation and depletion, respectively. The isosurface value is 0.002 |e| Å^{-3}.

configuration at η^2 mode found here is reasonable in comparison to the adsorption of CH_4 on differently active centers, *i.e.*, transition metal $[M(pyridine)_n]^{2+}$ complexes,[37] single-atom Fe-doped graphene and h-BN sheets,[38] and Cu^{n+} copper clusters.[39] However, in our case, the binding energy of methane on Cu^{2+} of ZIF-204 is at-most half of the methane binding energies on the structures mentioned above. The smaller interaction energy can be attributed to either the electronic properties of metal centers or the effect of coordinated ligands. Due to a weak electrostatic interaction, the PDOS of CH_4_ads/ZI and pristine ZI are almost similar, as shown in Fig. 4(d) and (b), respectively. It is possible for the activation of the C–H σ-bond by the metal active center, which was discussed in the previous work.[38] In this study, we found that the activated hydrogen atoms insert into Cu–N bonds, causing the hydrogenation of imidazole ligands. Those hydrogenated structures are unstable and are ignored in our current study.

3.2.2. CH_4 adsorption on ZI_O. There are two distinguished adsorption configurations for the adsorption of CH_4 over ZI_O denoted by CH_4_ads_s, oxo-side site, see Fig. 3(c), and CH_4_ads_t, oxo-top site, see Fig. 3(e). Both the adsorption processes are exothermic at the relative energies of 0.30 and 0.22 eV, as presented in Table 3, entries 2 and 3, respectively. The structural parameters for CH_4_ads_s and CH_4_ads_t are 1.94, 1.99, 1.10, and 1.95, 2.24, and 1.09(6) Å for CuO, OH_a, and CH_a, respectively. The bond lengths calculated here can be compared to values obtained for CH_4 adsorption on FeO-

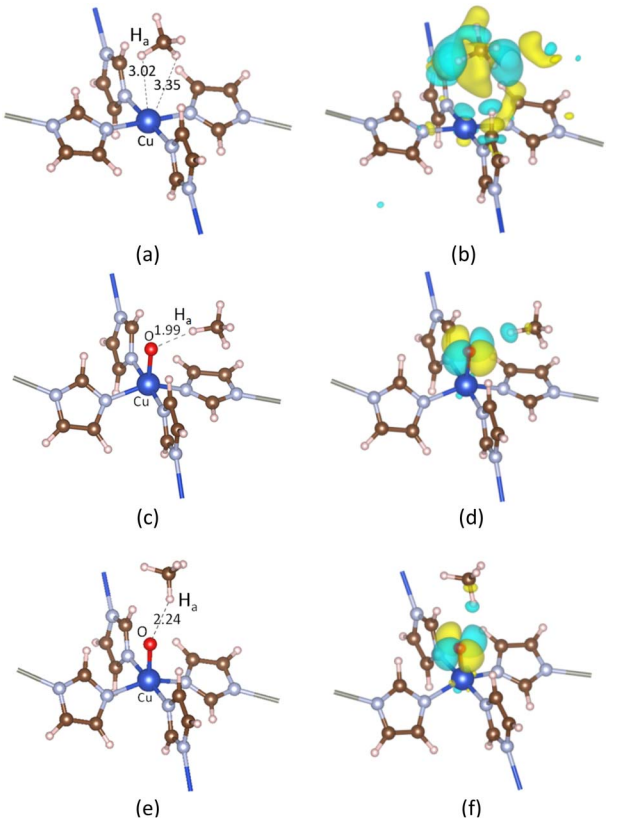

Fig. 3 Adsorption configurations and the corresponding EDD of CH_4 on ZI in (a) and (b), on ZI_O with the most stable in (c) and (d), and the second most stable in (e) and (f). H_a represents the hydrogen atom in CH_4 that is closest to the Cu center or the oxo ligand. The isosurface value is 0.002 |e| Å^{-3}.

Table 3 Adsorption sites and adsorption energies of CH_4 on ZI and ZI_O

No.	Structure	E_{ads} (eV)	Location
1	CH_4_ads/ZI	−0.24	Metal-top
2	CH_4_ads_s/ZI_O	−0.30	Oxo-side
3	CH_4_ads_t/ZI_O	−0.22	Oxo-top

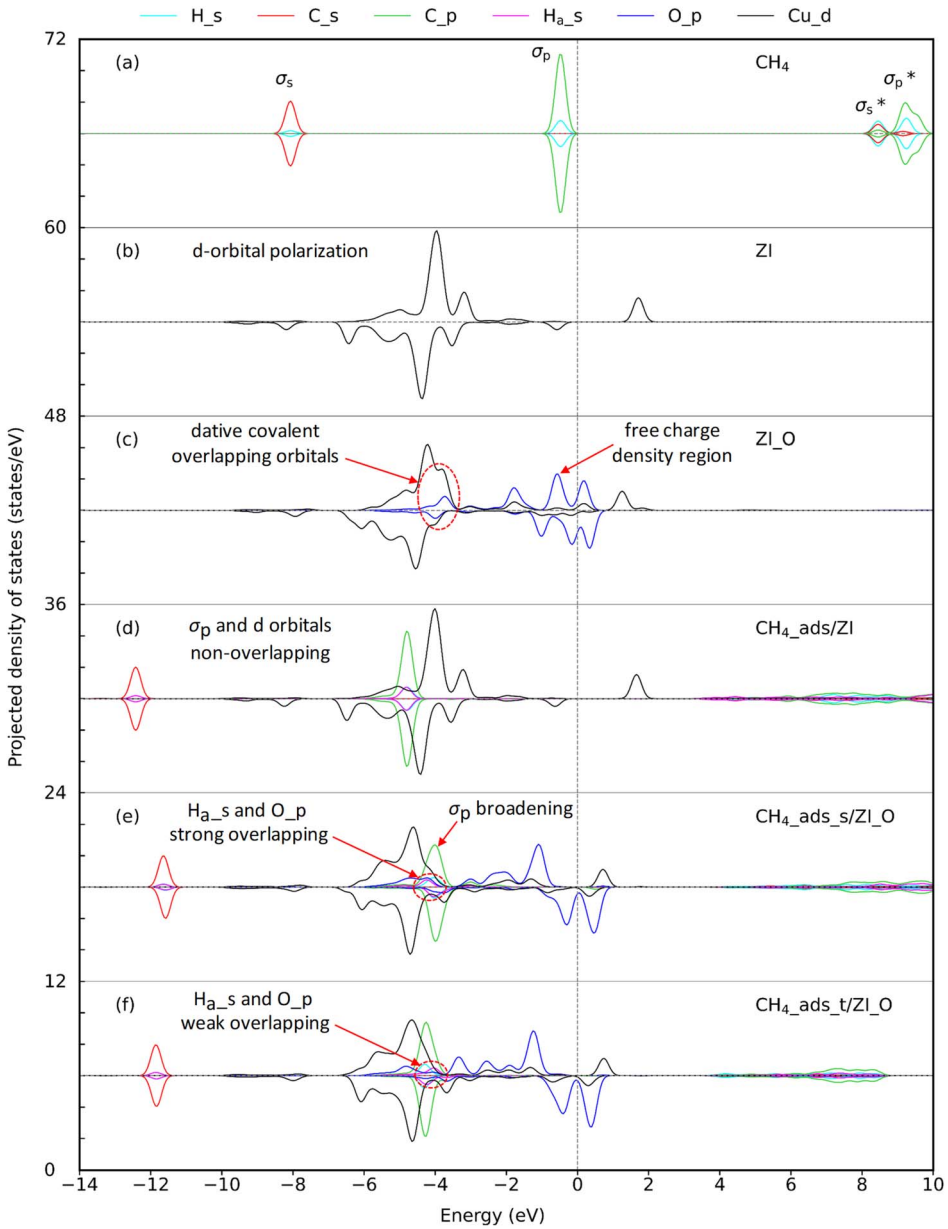

Fig. 4 Projected density of states (PDOS) for (a) isolated CH_4 molecule, (b) pristine ZIF-204 denoted as ZI, (c) oxo-doped ZIF-204 denoted as ZI_O, (d) CH_4 molecule adsorbed on ZI, (e) CH_4 molecule adsorbed on ZI_O at the side site, and (f) CH_4 molecule adsorbed on ZI_O at the top site. Lines in cyan, red, green, pink, blue, and black represent the PDOS of the s-orbital of H, s-orbital of C, and p-orbital of C in CH_4, s-orbital of the interacting H_a, p-orbital of oxo, and d-orbital of the copper, respectively. The dashed line crossing at 0 eV represents the Fermi level.

decorated graphene of 1.63, 2.46, and 1.10 Å for CuO, OH_a, and CH_a, respectively.[38] It can be seen that although the OH_a distance is longer for CH_4 on FeO than CuO, *i.e.*, 2.46 *vs.* 1.99 Å, the elongation of CH_a is the same with 1.10 Å. This disagreement could be attributed to the difference in electronic properties of Fe and Cu centers. A considerably shorter of OH_a distance and an obvious elongation of CH_a for CH_4 located at the oxo-side position compared to one at the top position demonstrate that the interaction between CH_4 and oxo is stronger for CH_4 residing on the oxo-side site. In addition, given an elongation of CH_a bond lengths, we also observe a decrease, about 200 cm^{-1}, of the stretching mode for CH_a bond in CH_4_ads_s compared to CH_4 in the gas phase, *i.e.*, 2888 cm^{-1} *vs.* 3095 cm^{-1}, respectively. The weaker CH_a bond in CH_4 arising from interacting with oxo is an important feature for the CH_4 activation. EDD plots in Fig. 3(d) and (f) show a similar distribution of charge for both adsorption configurations. In the presence of CH_4, the p orbital of oxo is split into different regions of the electron accommodation and depletion concerning O_p_x and O_p_y, while the electron on O_p_z orbital is unchanged. It is obvious that there is a slight loss of electron on the H atom of CH_4. This suggests a hydrogen bonding between CH_4 and the oxo species. PDOS in Fig. 4(e) shows a strong overlap region of O_p and H_a_s indicated by the same peak at

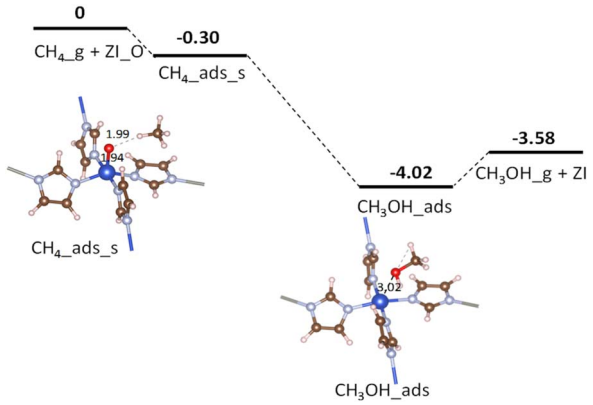

Fig. 5 Potential energy surface for CH_4 oxidation over ZI_O *via* the CH_4_ads_s pathway. Relative energies are given in eV. The zero-reference energy is the sum of the total energies of the isolated CH_4 molecule and ZI_O. Zero-point energy correction is not included.

around −4.0 eV demonstrating the existence of such hydrogen bonding. The PDOS in Fig. 4(f) also presents such overlap which is smaller due to weaker hydrogen-bonding interactions.

3.3. Oxidation of CH_4 over modified ZI

The overall catalytic reaction is proposed.

$$CH_4\_g + ZI\_O \rightarrow CH_3OH\_g + ZI \quad (4)$$

The detailed reaction mechanism follows:

$$CH_4\_g + ZI\_O \rightarrow CH_4\_ads + ZI\_O \quad (5)$$

$$CH_4\_ads + ZI\_O \rightarrow CH_3\_ads + ZI\_OH \quad (6)$$

$$CH_3\_ads + ZI\_OH \rightarrow CH_3OH\_ads + ZI \quad (7)$$

$$CH_3OH\_ads + ZI \rightarrow CH_3OH\_g + ZI \quad (8)$$

According to the overall reaction in eqn (4), ZI_O plays the role of a catalyst for transferring its oxo group to CH_4 to form CH_3OH molecules. The detail mechanism of this transfer is described in the subsequent eqn (5)–(8). The reaction initiates by the attachment of gas-phase molecule CH_4 onto the oxo group, shown in eqn (5). The following eqn (6) and (7) describe the activation of the C–H bond and the recombination of the C–O bond, respectively. Eqn (8) presents the desorption of the final product CH_3OH_ads into the gas phase.

Fig. 5 displays the potential energy surface for the CH_4_ads_s pathway. Calculated results from CI-NEB show that none of the proposed reaction steps in eqn (6) or eqn (7) attain intrinsic activation barriers (*cf.* Table 4, entry 1). Here, the C–H bond is weakened by the presence of the oxo group. After a total transfer of hydrogen atom to the oxo group to become Cu–OH moiety, the remaining induced methyl-like radical directly withdraw the hydroxyl OH group (in Cu–OH) to form the adsorbed CH_3OH molecule. The two reaction steps happen simultaneously without the introduction of any transition or intermediate states. It could be due to a strong hydrogen bonding between the oxo and H atom (in CH_4) making this bond weaken for the activation with a zero barrier. The broadening of the C–H (in CH_4) bonding band around −4.0 eV shown in Fig. 4(e) demonstrates a strong influence of O_p on the C–H σ-bond. Moreover, the short distance between the induced methyl-like radical and the Cu–OH moiety also facilitates its recombination for the final products. The absence of intermediates suggests that the above conversion reactions follow the concerted direct oxo insertion mechanism which has been discussed in early works.[40,41]

Fig. 6 shows the potential energy surface for the conversion of CH_4 into CH_3OH starting from the adsorption configuration CH_4_ads_t. It has been seen that there is only one transition state (TS) corresponding to the formation of the C–O bond, while the activation of the C–H bond is barrierless (see Table 4, entry 2). The energy barrier is found to be 0.16 eV (see Table 4, entry 3) for the transition from the intermediate Im to TS. For the TS, there is a unique imaginary frequency calculated to be 114.5 cm^{-1} associated with a concurrent rotation and translation of CH_3 radical towards the Cu–OH moiety. The energy profile for a C–O bond recombination is plotted in Fig. 7. The energy deviation is rather smooth with a small activation barrier found, demonstrating an appropriate transition from the initial Im state to TS, and to the final state CH_3OH_s. The presence of CH_3 radical in the Im state suggests that the CH_4_ads_t pathway follows hydrogen-atom abstraction radical rebound mechanism.[41,42] For such the mechanism, an early work on methane oxidation on pMMO-inspired trinuclear copper complex, $[Cu_3(\mu\text{-}O)_2(7\text{-}N\text{-}Etppz)]^+$, reported two transition states with moderate barriers of 0.33 and 0.38 eV for C–H bond dissociation and C–O bond recombination, respectively.[42] It can be also compared to low barriers of 0.23 eV for H-abstraction and 0.55 eV for methyl radical rebound revealed by Cao *et al.* for methane oxidation over PMMO-extracted monocopper sites.[11] The results found here are also more reasonable by a reference to a recent study on copper-doped ZIF-7, an inspired PMMO structure.[23] Accordingly, the active center O–CuN_4 moiety can

Table 4 Activation energies of involved reactions for both CH_4_ads_s and CH_4_ads_t pathways

Initial configuration	No.	Reaction step	Bond activation	Activation energy (eV)
CH_4_ads_s	1	CH_4_ads_s → CH_3OH_ads	C–H/C–O	0.00
CH_4_ads_t	2	CH_4_ads_t → Im	C–H	0.00
	3	Im → CH_3OH_ads	C–O	0.16

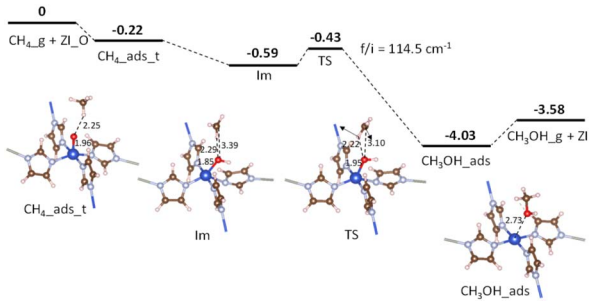

Fig. 6 Potential energy surface for CH_4 conversion over ZI_O *via* the CH_4_ads_t pathway. Relative energies are given in eV. The zero-reference energy is the sum of the total energies of the isolated CH_4 molecule and ZI_O. Zero-point energy correction is not included.

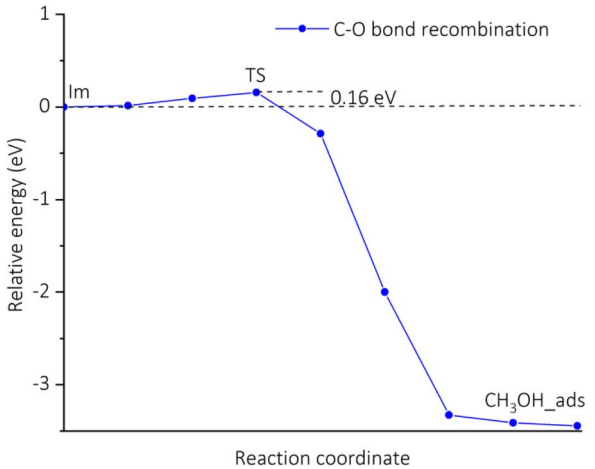

Fig. 7 Energy changes along the reaction coordinate for a C–O bond recombination *via* the CH_4_ads_t pathway calculated by the CI-NEB method.

oxidize CH_4 by going through two reaction steps similar to our aforementioned mechanism with negligible activation barriers, *i.e.*, 0.08 eV for the C–H bond dissociation and 0.0 eV for the C–O bond recombination.[23] It is worth mentioning here that transition barriers are negligible regardless of whether the methane oxidation proceeds *via* either pathways.

4. Conclusions

We study the direct conversion of methane to methanol over modified ZIF-204 metal–organic frameworks by means of first-principle DFT-based calculations. The catalytic activity of the modified ZIF-204 is identified by the oxo-deposited species at monocopper sites. In pristine ZIF-204, methane molecules physisorb on the open monocopper sites with the adsorption energy of 0.24 eV. The activation of methane over these copper centers is beyond the interest of the current study due to a weak electrostatic interaction between methane and metal cation and also the instability of the induced hydrogenation structures. In oxo-doped ZIF-204, different reaction mechanisms are found to be affected by the adsorption behavior of methane molecules towards oxo groups through hydrogen bondings with oxo groups. The oxo plays the key role as a reactive center for the activation of methane *via* either the concerted direct oxo insertion or the hydrogen-atom abstraction radical rebound mechanism. The conversion reactions occur without energy barriers for the concerted pathway or with a negligible transition barrier of 0.16 eV for the C–O bond recombination for the abstraction radical rebound pathway. The reactions happen easily in response to strong catalytic activities of the oxo-oxidizing doped species. Those negligible energy barriers propose a favorable kinetic for the direct oxidation of methane over modified ZIF-204 metal–organic structures.

Conflicts of interest

There are no conflicts to declare.

Acknowledgements

This research was funded by Vietnam National University Ho Chi Minh City (VNU-HCM) under grant number C2022-50-03. Y. K. was supported by Suranaree University of Technology (SUT), Thailand Science Research and Innovation (TSRI), and National Science, Research and Innovation Fund (NSRF) (NRIIS Project Number 90465). The authors would like to acknowledge colleagues from Institute for Materials Research, Tohoku University, Japan, Institute of Atomic and Molecular Sciences, Academia Sinica, Taiwan, and Key Laboratory for Multiscale Simulation of Complex Systems, University of Science, Vietnam National University-Hanoi, Hanoi for their help in providing and maintaining high-performance computing resources. T. N. M. L. would also like to thank Dr Jer-Lai Kuo at Institute of Atomic and Molecular Sciences, Academia Sinica, Taiwan and Dr Cheng-Chau Chiu at National Sun Yat-Sen University, Taiwan for assistance and fruitful discussions.

References

1 L. S. Andrade, H. H. L. B. Lima, C. T. P. Silva, W. L. N. Amorim, J. G. R. Poço, A. López-Castillo, M. V. Kirillova, W. A. Carvalho, A. M. Kirillov and D. Mandelli, *Coord. Chem. Rev.*, 2023, **481**, 215042.
2 N. F. Dummer, D. J. Willock, Q. He, M. J. Howard, R. J. Lewis, G. Qi, S. H. Taylor, J. Xu, D. Bethell, C. J. Kiely and G. J. Hutchings, *Chem. Rev.*, 2022, **123**(9), 6359–6411.
3 V. C. Wang, S. Maji, P. P. Chen, H. K. Lee, S. S. Yu and S. I. Chan, *Chem. Rev.*, 2017, **117**, 8574–8621.
4 A. A. Latimer, A. Kakekhani, A. R. Kulkarni and J. K. Nørskov, *ACS Catal.*, 2018, **8**, 6894–6907.
5 M. Ravi, M. Ranocchiari and J. A. van Bokhoven, *Angew. Chem., Int. Ed.*, 2017, **56**, 16464–16483.
6 Y. Tsuji and K. Yoshizawa, *J. Phys. Chem. C*, 2018, **122**, 15359–15381.
7 Z. Liu, E. Huang, I. Orozco, W. Liao, R. M. Palomino, N. Rui, T. Duchon, S. Nemsak, D. C. Grinter, M. Mahapatra, P. Liu, J. A. Rodriguez and S. D. Senanayake, *Science*, 2020, **368**, 513–517.

8 Z. Liang, T. Li, M. Kim, A. Asthagiri and J. F. Weaver, *Science*, 2017, **356**, 299–303.
9 M. O. Ross, F. MacMillan, J. Wang, A. Nisthal, T. J. Lawton, B. D. Olafson, S. L. Mayo, A. C. Rosenzweig and B. M. Hoffman, *Science*, 2019, **364**, 566–570.
10 K. Yoshizawa and Y. Shiota, *J. Am. Chem. Soc.*, 2006, **128**, 9873–9881.
11 L. Cao, O. Caldararu, A. C. Rosenzweig and U. Ryde, *Angew. Chem., Int. Ed.*, 2018, **57**, 162–166.
12 K. Narsimhan, K. Iyoki, K. Dinh and Y. Roman-Leshkov, *ACS Cent. Sci.*, 2016, **2**, 424–429.
13 A. R. Kulkarni, Z.-J. Zhao, S. Siahrostami, J. K. Nørskov and F. Studt, *ACS Catal.*, 2016, **6**, 6531–6536.
14 V. L. Sushkevich and J. A. van Bokhoven, *ACS Catal.*, 2019, **9**, 6293–6304.
15 M. B. Park, E. D. Park and W. S. Ahn, *Front. Chem.*, 2019, **7**, 514.
16 U. Engedahl, A. Boje, H. Ström, H. Grönbeck and A. Hellman, *J. Phys. Chem. C*, 2021, **125**, 14681–14688.
17 X. Tang, L. Wang, B. Yang, C. Fei, T. Yao, W. Liu, Y. Lou, Q. Dai, Y. Cai, X.-M. Cao, W. Zhan, Y. Guo, X.-Q. Gong and Y. Guo, *Appl. Catal., B*, 2021, **285**, 119827.
18 T. Ikuno, J. Zheng, A. Vjunov, M. Sanchez-Sanchez, M. A. Ortuno, D. R. Pahls, J. L. Fulton, D. M. Camaioni, Z. Li, D. Ray, B. L. Mehdi, N. D. Browning, O. K. Farha, J. T. Hupp, C. J. Cramer, L. Gagliardi and J. A. Lercher, *J. Am. Chem. Soc.*, 2017, **139**, 10294–10301.
19 J. Baek, B. Rungtaweevoranit, X. Pei, M. Park, S. C. Fakra, Y. S. Liu, R. Matheu, S. A. Alshmimri, S. Alshehri, C. A. Trickett, G. A. Somorjai and O. M. Yaghi, *J. Am. Chem. Soc.*, 2018, **140**, 18208–18216.
20 J. Zheng, J. Ye, M. A. Ortuno, J. L. Fulton, O. Y. Gutierrez, D. M. Camaioni, R. K. Motkuri, Z. Li, T. E. Webber, B. L. Mehdi, N. D. Browning, R. L. Penn, O. K. Farha, J. T. Hupp, D. G. Truhlar, C. J. Cramer and J. A. Lercher, *J. Am. Chem. Soc.*, 2019, **141**, 9292–9304.
21 D. Li, H.-Q. Xu, L. Jiao and H.-L. Jiang, *Energy Chem.*, 2019, **1**(1), 100005.
22 A. S. Rosen, J. M. Notestein and R. Q. Snurr, *ACS Catal.*, 2019, **9**, 3576–3587.
23 H. Lee, C. Kwon, C. Keum, H.-E. Kim, H. Lee, B. Han and S.-Y. Lee, *Chem. Eng. J.*, 2022, **450**, 138472.
24 N. T. Nguyen, T. N. Lo, J. Kim, H. T. Nguyen, T. B. Le, K. E. Cordova and H. Furukawa, *Inorg. Chem.*, 2016, **55**, 6201–6207.
25 G. Kresse and J. Hafner, *Phys. Rev. B: Condens. Matter Mater. Phys.*, 1993, **47**, 558–561.
26 J. P. Perdew, K. Burke and M. Ernzerhof, *Phys. Rev. Lett.*, 1997, **78**, 1396.
27 J. P. Perdew, K. Burke and M. Ernzerhof, *Phys. Rev. Lett.*, 1996, **77**, 3865–3868.
28 S. Grimme, S. Ehrlich and L. Goerigk, *J. Comput. Chem.*, 2011, **32**, 1456–1465.
29 P. E. Blöchl, *Phys. Rev. B: Condens. Matter Mater. Phys.*, 1994, **50**, 17953–17979.
30 M. Cococcioni and S. de Gironcoli, *Phys. Rev. B: Condens. Matter Mater. Phys.*, 2005, **71**(3), 035105.
31 G. Kresse and D. Joubert, *Phys. Rev. B: Condens. Matter Mater. Phys.*, 1999, **59**, 1758–1775.
32 Y. Zhang and W. Yang, *Phys. Rev. Lett.*, 1998, **80**, 890.
33 B. Hammer, L. B. Hansen and J. K. Nørskov, *Phys. Rev. B: Condens. Matter Mater. Phys.*, 1999, **59**, 7413–7421.
34 S. Maintz, V. L. Deringer, A. L. Tchougreeff and R. Dronskowski, *J. Comput. Chem.*, 2016, **37**, 1030–1035.
35 G. Henkelman, B. P. Uberuaga and H. Jónsson, *J. Chem. Phys.*, 2000, **113**, 9901–9904.
36 K. Momma and F. Izumi, *J. Appl. Crystallogr.*, 2011, **44**, 1272–1276.
37 G. W. Roffe and H. Cox, *J. Phys. Chem. A*, 2013, **117**, 3017–3024.
38 S. Impeng, P. Khongpracha, J. Sirijaraensre, B. Jansang, M. Ehara and J. Limtrakul, *RSC Adv.*, 2015, **5**, 97918–97927.
39 O. V. Lushchikova, S. Reijmer, P. B. Armentrout and J. M. Bakker, *J. Am. Soc. Mass Spectrom.*, 2022, **33**, 1393–1400.
40 D. Balcells, E. Clot and O. Eisenstein, *Chem. Rev.*, 2010, **110**, 749–823.
41 P. P. Chen and S. I. Chan, *J. Inorg. Biochem.*, 2006, **100**, 801–809.
42 C. H. Yeh, S. S. F. Yu, S. I. Chan and J. C. Jiang, *ChemistrySelect*, 2018, **3**, 5113–5122.